AIAA JOURNAL
Vol. 40, No. 3, March 2002

Numerical Simulation of Two-Dimensional Blade–Vortex Interactions Using Unstructured Adaptive Meshes

Woo Seop Oh,* Joo Sung Kim,* and Oh Joon Kwon†
Korea Advanced Institute of Science and Technology, Taejon 305-701, Republic of Korea

A two-dimensional Euler flow solver has been developed for the simulation of unsteady, blade–vortex interaction problems on unstructured meshes. The Euler solver is based on a second-order-accurate implicit time integration using a point Gauss–Seidel relaxation scheme and a dual time-step subiteration. A vertex-centered, finite volume discretization is used in conjunction with the Roe's flux-difference splitting. An unsteady solution-adaptive dynamic mesh scheme is used by adding and deleting mesh points at every adaptation step to take account of not only spatial but also of temporal variations of the flowfield. Unsteady flow around a harmonically oscillating airfoil and traveling vortex in a freestream were simulated to validate the accuracy of the dynamic mesh adaptation procedure. Three blade–vortex interaction problems, two at transonic freestream speeds and one with vortex–airfoil collision, were investigated. Computed results show good agreements with existing experimental and computational results within the accuracy of the present inviscid solver. It is found that the evolution of vorticies and propagation of acoustic waves can be accurately simulated using the present unstructured dynamic mesh adaptation procedure.

Introduction

THE blade–vortex interaction (BVI) phenomenon contains one of the most complex unsteady flow features of helicopter rotor blades in forward flight. Helicopter BVI occurs when the trailing tip vortices are ingested into the rotor disk during descending flight or maneuver. The interaction induces sudden changes in aerodynamic loading, which results in blade vibration and aeroelastic instability. It also generates a highly directional impulsive noise.

Numerical simulation of BVI problems has been of interest to computational fluid dynamics (CFD) researchers for many years. Different levels of numerical complexity have been adopted depending on available computational resources and numerical algorithms.[1–7] At the same time, experimental studies have been performed for the investigation of BVI problems in parallel to the computational approaches. These provided a better understanding of the physics and offered validation bases for computational results.[3,8,9]

Several difficulties exist concerning an accurate numerical prediction of BVI. One of the most prominent problems encountered is the inherent numerical dissipation contained in CFD codes, which severely restricts preserving the strength of vortices, particularly at the flow region where the grid resolution is not well established, such as far upstream away from the airfoil. Thus, numerical methods based on structured meshes usually rely on special treatments such as the perturbation method[10,11] or the vorticity confinement method.[12] However, the perturbation method is not suitable for strong interactions such as vortex–airfoil collisions. The vorticity confinement method, which is similar to using an artificial viscosity for central-difference schemes, is not robust. Recently, several researchers attempted to use high-order schemes[4,13–15] to relieve this difficulty, which at the same time accompanies numerical problems in the form of poor convergence for the computation of transonic BVI cases. Numerical dissipation also affects the accurate capturing of shock wave behaviors, especially when the traveling vortex strongly interacts with it.

An alternative approach to relieving the difficulty associated with the numerical dissipation is to use solution-adaptive mesh methodology[16–18] to capture the local details of the vortex structure and its interaction with the airfoil within reasonable computational costs. Ng and Hillier[19] used a local mesh refinement technique and an embedded mesh method on structured meshes. However, their mesh adaptation technique was not fully solution adaptive in a sense that the adaptation followed a prescribed vortex passage presumed in advance. The first attempt at a dynamic mesh adaptation technique applied for a transonic BVI simulation on unstructured meshes was made by Hwang and Kuo.[20] They demonstrated that the numerical dissipation can be reduced, and the aeroacoustic behavior can be well-resolved on an explicit high-order scheme combined with a solution-adaptive grid approach. Their approach includes the Runge–Kutta time-integration method and Roe's Riemann solver with a MUSCL-type differencing. However, their grid adaptation was limited to two levels to avoid too much grid skewness and to maintain reasonably good grid quality resulting from the simple mesh refinement procedure. Therefore, a relatively fine initial mesh was required to achieve desired accuracy.

In the present study, a two-dimensional implicit Euler solver was developed for the efficient and accurate numerical simulation of BVI problems on unstructured meshes. The Euler solver is based on a vertex centered finite volume method with Roe's flux-difference splitting.[21] The governing equations are integrated in time using an implicit time-marching method. The subiteration and dual time stepping have been incorporated,[22] which retain second-order accuracy in time. For accurate capturing of the vortex structure and acoustic signal, a multilevel solution-adaptive dynamic mesh refinement technique is used[17] combined with an improved mesh-enrichment indicator. Good grid quality is always maintained even after several levels of mesh adaptation by using a temporary cell approach. The dynamic mesh adaptation procedure has been demonstrated for flow around a harmonically oscillating airfoil. A traveling vortex in a freestream was also evaluated to validate the effect of mesh adaptation for preserving the vortex strength on the present second-order spatially accurate solver. Then, two transonic BVI problems and a vortex–airfoil collision case were investigated and compared with existing numerical and experimental results.

Numerical Method

Governing Equations

The flow motion is governed by the two-dimensional, time-dependent Euler equations for an ideal gas that express the conservation of mass, momentum, and energy for a Newtonian fluid in the absence of external forces. The equations are given hereafter in

Received 28 November 2000; revision received 5 July 2001; accepted for publication 10 July 2001.

*Doctoral Candidate, Department of Aerospace Engineering, 373-1 Kusong-Dong, Yusong-Gu.

†Associate Professor, Department of Aerospace Engineering, 373-1 Kusong-Dong, Yusong-Gu, Senior Member AIAA.

an integral form for an arbitrary domain of computation Ω with the boundary of domain $\partial\Omega$:

$$\frac{\partial}{\partial t}\int_{\Omega} \boldsymbol{Q}\,\mathrm{d}A + \oint_{\partial\Omega} F(\boldsymbol{Q},\boldsymbol{n})\,\mathrm{d}S = 0 \tag{1}$$

where $\boldsymbol{Q}$ is the vector of conservative variables and $F(\boldsymbol{Q},\boldsymbol{n})$ is the inviscid flux vector in standard conservation form:

$$\boldsymbol{Q} = \begin{bmatrix} \rho \\ \rho u \\ \rho v \\ e_0 \end{bmatrix}, \qquad F(\boldsymbol{Q},\boldsymbol{n}) = \begin{bmatrix} \rho V_r \\ \rho u V_r + p n_x \\ \rho v V_r + p n_y \\ (e_0 + p)V_r + p V_g \end{bmatrix}$$

Here n_x and n_y are the Cartesian components of the exterior surface unit outward normal vector $\boldsymbol{n}$ on the boundary $\partial\Omega$, ρ is density, and u and v are Cartesian velocity components in the inertial coordinate frame. V_r is the normal component of the relative velocity vector and $\boldsymbol{V}_g$ is the grid velocity vector:

$$V_r = (\boldsymbol{V} - \boldsymbol{V}_g)\cdot\boldsymbol{n}, \qquad V_g = \boldsymbol{V}_g \cdot \boldsymbol{n}$$

The term e_0 is the total energy per unit volume. These equations are nondimesionalized by the freestream density, the freestream speed of sound, and the airfoil chord length. Equation (1) describes a relationship where the time rate of change of the state vector $\boldsymbol{Q}$ within the domain Ω is balanced by the net flux F across the boundary $\partial\Omega$.

Discretization

The governing equation (1) is discretized spatially using a finite volume scheme. The domain is divided into a finite number of control volumes composed of median duals surrounding each vertex as shown in Fig. 1. Equation (1) is applied at each control volume, and the flow variables are stored at the vertex point. The discretized form of Eq. (1) for each individual vertex-centered control volume i and dual face j becomes

$$A_i \frac{\partial \boldsymbol{Q}_i}{\partial t} + \sum_{j}^{N\,\text{face}} (F_j) = 0, \qquad i = 1, 2, 3, \ldots \tag{2}$$

where N face represents the total number of dual faces surrounding the current control volume A_i. The inviscid flux across each face j is computed using Roe's flux-difference splitting formula[21]:

$$F_j = \tfrac{1}{2}[F(\boldsymbol{Q}_L) + F(\boldsymbol{Q}_R) - |\tilde{A}|(\boldsymbol{Q}_R - \boldsymbol{Q}_L)]_j \tag{3}$$

where $\boldsymbol{Q}_L$ and $\boldsymbol{Q}_R$ are the conservative variables at the left and right sides of a dual face j. The flow variables at each dual face are computed using a linear reconstruction approach that is second-order accurate in space. In this approach, face value of the primitive variables is calculated from surrounding vertices using the averaged solution gradient of each control volume obtained from a least-squares procedure.[23] The matrix $\tilde{A}$ is evaluated with Roe-averaged quantities. Venkatakrishnan's limiter[24] is used to reduce the numerical oscillation for transonic BVI problems.

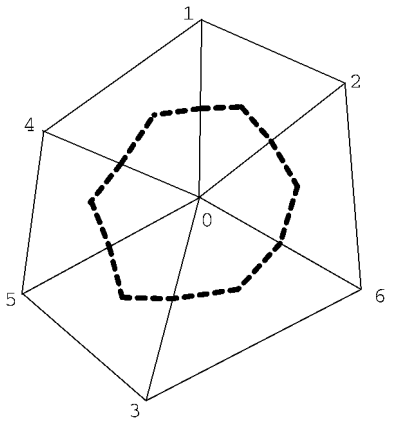

Fig. 1 Definition of control volume: - - -, median dual.

Implicit Time Integration

The discretized equation (2) can be rewritten as a set of differential equations:

$$A_i \frac{\partial \boldsymbol{Q}_i}{\partial t} + R(\boldsymbol{Q}_i) = 0, \qquad i = 1, 2, 3, \ldots \tag{4}$$

where $R(\boldsymbol{Q}_i)$ is the residual that denotes the numerical approximation of the inviscid flux in Eq. (2).

An implicit time integration algorithm based on the linearized Euler backward time differencing is used to update the solution in time. The time derivative term is linearized as follows[25]:

$$\frac{\partial \boldsymbol{Q}_i}{\partial t} = \frac{2+\phi}{2}\frac{\Delta \boldsymbol{Q}}{\Delta t} + \frac{2+\phi}{2}\frac{\boldsymbol{Q}^p - \boldsymbol{Q}^n}{\Delta t} - \frac{\phi}{2}\frac{\boldsymbol{Q}^n - \boldsymbol{Q}^{n-1}}{\Delta t} \tag{5}$$

where $\Delta\boldsymbol{Q} = \boldsymbol{Q}^{n+1} - \boldsymbol{Q}^n$ and the parameter ϕ controls the temporal order of accuracy. The scheme is first-order accurate in time if $\phi = 0$ and second-order accurate for $\phi = 1$. By evaluating the residual $R(\boldsymbol{Q}_i)$ at the time level $'n+1'$ and using a Newton-type linearization of the fluxes, Eq. (4) can be written for a given control volume i, its dual faces j, and adjacent control volume k as

$$\left[D_i \Delta \boldsymbol{Q}_i + \sum_{j}^{N\,\text{face}} S_{j,k} \Delta \boldsymbol{Q}_k \right]^{n+1,p} = -\boldsymbol{Q}_t - R(\boldsymbol{Q}_i)^{n+1,p} \tag{6}$$

where

$$D_i = \frac{2+\phi}{2}\frac{A_i}{\Delta t} + \sum_{j}^{N\,\text{face}} S_{j,i}$$

$$\boldsymbol{Q}_t = \frac{A_i}{\Delta t}\left(\frac{2+\phi}{2}\boldsymbol{Q}^{n+1,p} - \frac{2+2\phi}{2}\boldsymbol{Q}^n + \frac{\phi}{2}\boldsymbol{Q}^{n-1} \right)$$

A_i is the area of control volume, $S_{j,k} = \partial \hat{F}_j / \partial \boldsymbol{Q}_k$, and $\Delta\boldsymbol{Q} = \boldsymbol{Q}^{n+1,p+1} - \boldsymbol{Q}^{n+1,p}$. The superscript p denotes the subiteration index. D_i and $S_{j,k}$ are the diagonal and off-diagonal terms of the flux Jacobian. The dual time stepping is also used to eliminate linearization errors. The inviscid flux Jacobian is evaluated using the Roe-averaged[21] values as follows:

$$\frac{\partial F_j}{\partial \boldsymbol{Q}_i} = \frac{1}{2}\left[\frac{\partial F(\boldsymbol{Q}_L)}{\partial \boldsymbol{Q}_L} + |\tilde{A}| \right], \qquad \frac{\partial F_j}{\partial \boldsymbol{Q}_k} = \frac{1}{2}\left[\frac{\partial F(\boldsymbol{Q}_R)}{\partial \boldsymbol{Q}_R} - |\tilde{A}| \right] \tag{7}$$

The resulting linear system of equations are solved at each time step using a point Gauss–Seidel method.

To simulate traveling vortex in a freestream and BVI problems, the vortex is initially described by an analytical form suggested by Scully (see Ref. 10). The nondimensional angular velocity of the initial vortex is expressed as

$$v_\theta = (\Gamma/2\pi r)\left[r^2 \Big/ \left(r^2 + a_c^2 \right) \right] \tag{8}$$

where a_c and r represent the core radius and the radial distance from the vortex center, respectively. The vortex strength Γ is normalized by the product of freestream Mach number, freestream speed of sound, and the airfoil chord length. The counterclockwise vortex is defined as positive.

The initial pressure and density fields can be evaluated using the radial momentum equation in conjunction with the energy equation for constant enthalpy flows.[11]

Dynamic Mesh Adaptation

To improve the accuracy of the flow simulation and to reduce the inherent numerical dissipation, a solution-adaptive grid scheme is applied. Grid points are dynamically added and deleted on the existing unstructured mesh at every adaptation level as detected by error indicators that are based on the estimation of local truncation error.

Error Indicator

There are a number of flow parameters that can be used as an error indicator. For steady flows, a specific and common example of error indicator is the magnitude of the density gradient $|\nabla\rho|$, which is a measure of spatial variation of the solution. However, for unsteady flows, a measure is needed that takes account of not only spatial but also temporal variations of the solution. For this reason, Rausch et al.[17] suggested the absolute value of the substantial derivative of density $|\mathrm{D}\rho/\mathrm{D}t|$ as an enrichment indicator. Hwang and Kuo[20] introduced a new mesh-enrichment indicator developed from the continuity equation, which is the absolute value of the gradient of the substantial derivative of density:

$$\left|\nabla\left(-\frac{1}{\rho}\frac{\mathrm{D}\rho}{\mathrm{D}t}\right)\right| = |\nabla(\nabla\cdot\boldsymbol{V})| \tag{9}$$

For the accurate and efficient capturing of shock, vortex, and acoustic signal, both the density gradient and the gradient of the substantial derivative of density in Eq. (9) are used as error indicators in the present study. The vorticity gradient is also used as an additional error indicator so that cells inside the traveling vortex core can be further refined to help maintain the strength of vortex.

To prevent an overrefinement due to small numerical fluctuation of the solution, different levels of error indicators are applied for cells inside and outside the region of 2–6 times the core radius from the vortex center. The center of the vortex core is approximately located by searching the local vorticity maximum within one-half of the vortex core radius from the vortex core center obtained from the previous time level.

Mesh Enrichment and Coarsening

Dynamic mesh adaptation is initiated on a relatively coarse mesh, and the cell division continues until a given criterion is satisfied. The error indicator is computed at each cell face and the value is examined to decide whether the particular face should be divided into smaller faces. Then, new node points are added at the center of targeted faces. Flow variables at the new node point are set as an average of the two node values attached to the face. When boundary faces are divided, a special treatment has to be applied to confirm that the coordinates of added node points recover the smooth curvature of the original geometry. In the present study, the Hermite polynomial interpolation method is adopted such that C0 and C1 continuities between the neighboring boundary faces are guaranteed.

Targeted cells are divided into either four normal subcells or two temporary subcells. To avoid the generation of highly stretched cells, temporary subcells are restricted from further subdivision. If an additional division is detected at the face of a temporary subcell and if the face is the one retained from its parent cell, the original cell is restored from the temporary subcells and then divided into four normal subcells as shown in Fig. 2. If the detected face belongs to the side of temporary subcells already divided from the parent cell, the original cell is divided into four normal subcells, and then the subcell, containing the detected face is again divided into two temporary subcells.

To increase the grid efficiency and to minimize the computational cost, a mesh coarsening procedure is also adopted in parallel to the mesh enrichment whenever the error indicator at local region of the flow diminishes due to changing flow characteristics in time. During the mesh coarsening procedure, previously added node points and subdivided cells are deleted from the grid connectivity array and the original cells are restored. The mesh enrichment history, the so-called historic coarsening, stored in the tree data structure is used for this purpose. The original mesh is not allowed to experience further coarsening.

Results and Discussion

The main objective of the present study is to assess the solution accuracy of the algorithm and the numerical methodology just described for the numerical simulation of BVI problems on unstructured meshes. Initially, the dynamic solution-adaptive mesh methodology was tested for flow around a harmonically oscillating airfoil. Also, a traveling vortex in a freestream was computed to evaluate the solution accuracy of the present solver. Then, the present numerical method and the dynamic mesh adaptation algorithm were validated for several BVI problems. The flow physics in close vortex–airfoil interactions were studied.

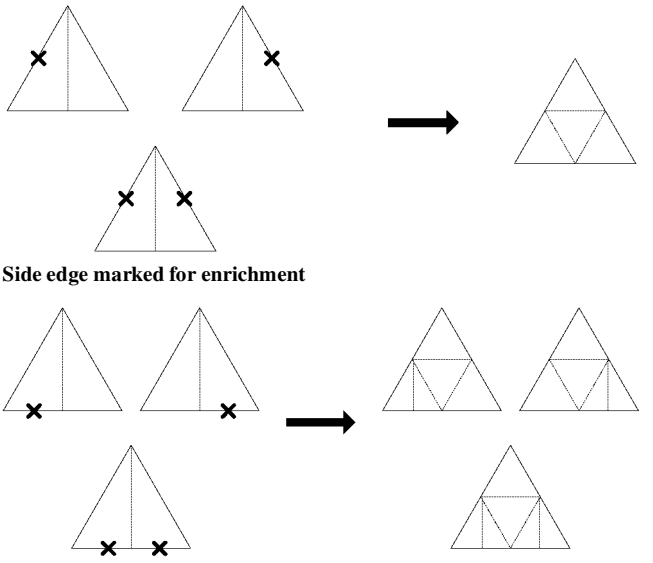

Fig. 2 Diagrams of mesh enrichment possibilities of temporary cells.[17]

Harmonically Oscillating Airfoil

For the initial validation, calculation was performed for flow around a NACA0012 airfoil section undergoing a harmonically oscillating motion at low angles of attack. The reduced frequency k of the oscillation based on the airfoil semichord length and the freestream velocity is 0.0814. The mean angle of attack α_0 is 0.016 deg, and the amplitude of oscillation α_1 is 2.51 deg. The freestream Mach number M_∞ is 0.755. The unstructured mesh is rigidly attached on the airfoil and rotates about the airfoil quarter-chord following the motion of the airfoil. Initially, steady-state solution is obtained at the mean angle of attack, and then the unsteady calculation is triggered. Calculation is performed for two cycles of the motion to obtain a periodic solution, which takes 5000 time steps per cycle. The dynamic mesh enrichment and coarsening is applied at every 10 time steps.

Instantaneous meshes at four different stages in time during the second cycle of the motion are shown in Fig. 3a. It is shown that the mesh enrichment and coarsening sequence captures the moving shock wave well for both its location and strength as it moves back and forth on the upper and lower surfaces of the airfoil. The corresponding surface pressure distributions are compared with experimental data[26] as shown in Fig. 3b. The overall agreements are good within the accuracy of the present inviscid solver. Comparison of the integrated normal force variation with the experimental data is made in Fig. 4 as a function of angle of attack. The results from other existing inviscid calculations[18,25] are also presented in Fig. 4. It is observed that the calculated normal force coefficient compares well with other results for both its magnitude and the mean slope.

Traveling Vortex in a Freestream

As the second validation case, convection of a free vortex in a uniform stream at a Mach number of 0.5 was tested. The accuracy of the present solution-adaptive unstructured mesh flow solver was compared to that of other high-order structured grid flow solvers.[14,15] The size of nomalized computational domain is 20×2, and the flowfield is divided uniformly into isotropic triangular elements containing 16,346 cells and 8469 node points. The traveling vortex has a core radius of 0.05 and a nondimensionalized strength of -0.2. It is initialized upstream of the flow, and the computation is proceeded until the vortex reaches 10 normalized distance downstream (200 times the vortex core radius). The size of the time step used for the calculation is 0.002. During the calculation, the initial mesh is dynamically refined by using the present solution-adaptive approach

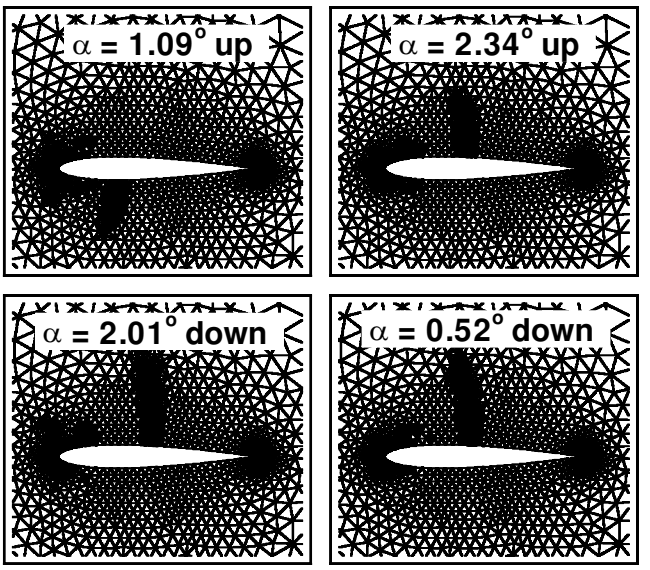

a) Instantaneous meshes

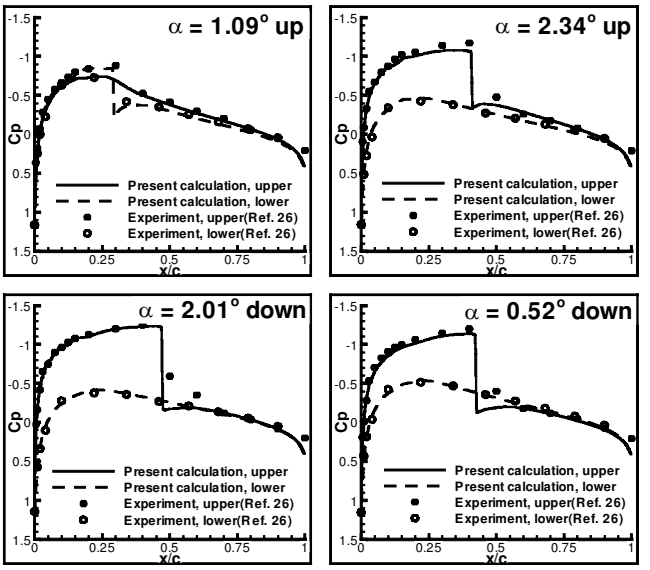

b) Instantaneous pressure distributions

Fig. 3 Instantaneous meshes and pressure distributions of a NACA0012 airfoil oscillating at $M_\infty = 0.755$, $\alpha_0 = 0.016$ deg, $\alpha_1 = 2.51$ deg, and $k = 0.0814$.

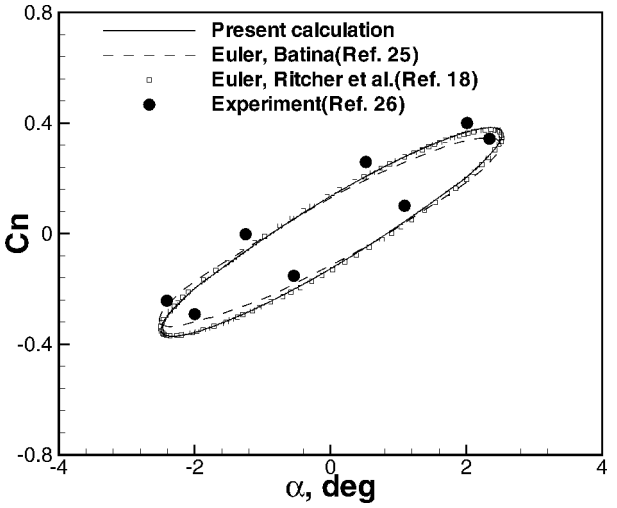

Fig. 4 Comparison of normal force coefficients vs instantaneous angle of attack of an oscillating NACA0012 airfoil.

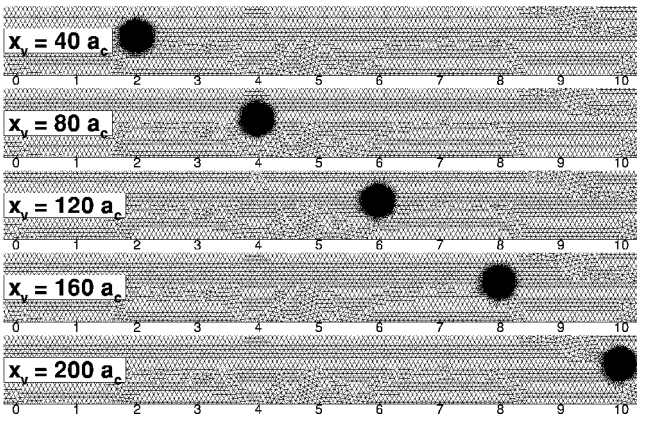

a) Instantaneous adapted meshes

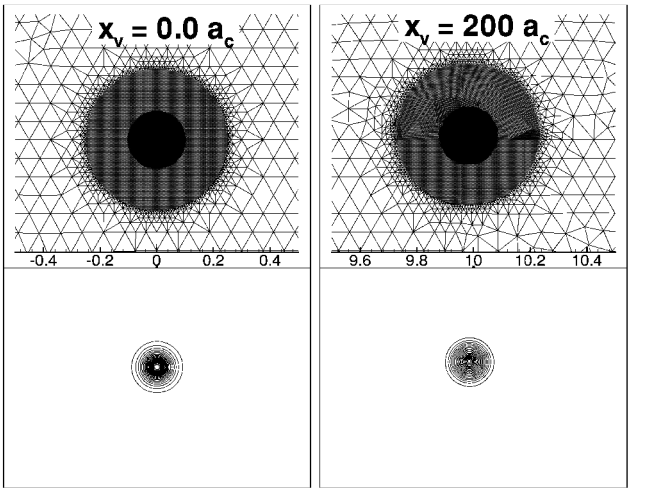

b) Partial view of instantaneous adapted meshes and vorticity contours

Fig. 5 Instantaneous meshes and vorticity contours for traveling vortex in a freestream for $M_\infty = 0.5$, $a_c = 0.05$, and $\Gamma = -0.2$.

until the targeted face length becomes smaller than 0.006. An additional level of mesh refinement is made inside the vortex core region to minimize the numerical dissipation. The mesh is spatially adapted every five time steps. The error indicator is calculated based on the vorticity gradient.

Figure 5a shows the history of vortex migration at several time frames with respect to the vortex position X_v. The mesh enrichment and coarsening following the trajectory of the vortex are well demonstrated. The average number of cells and node points are approximately 48,400 and 24,500, respectively, with 32 node points across the vortex core during the calculation. The total elapsed computational time is approximately 22.6 h on a personal computer with a Pentium II 500 processor. In Fig. 5b, meshes and vorticity contours around the vortex at the initial stage and at the end of computation are enlarged and compared. An additional level of mesh refinement inside the vortex core is also shown in the Fig. 5b. The vorticity contours at the two time levels visually confirm that the identity and the strength of the vortex core are well maintained after a significant distance of convection. Figure 6 represents the decay of the normalized peak-to-peak vertical velocity across the vortex core, $\Delta v/\Delta v_0$, with respect to the vortex convection distance. When an additional mesh refinement is not applied at the vortex core (case 1), approximately 8% decay of the initial peak-to-peak vertical velocity is observed after the vortex is convected 10 normalized distances downstream from the initial position. When the vortex core is refined one more level (case 2), the decay is reduced to less than 3%. The results are compared with those of piecewise quadratic reconstruction schemes with fourth- and eighth-order compact central evaluation of nodal derivatives obtained by Tang and Baeder.[15] It is shown that the present second-order-accurate

solution-adaptive mesh methodology represents slightly better results than the third-order-accuratescheme. The comparisons clearly demonstrate the solution accuracy of the present unstructured solution-adaptive mesh methodology for problems involving vortex dynamics where the numerical preservation of vorticity is critical. The mesh refinement of case 2 has been used for the study of following BVI problems.

Simulation of BVIs

At first, a transonic BVI problem was investigated at a freestream Mach number of 0.8 and a blade–vortex offset of $-0.26c$, where c is the chord length. The vortex has a core radius of $0.05c$ and a nondimensional strength of -0.2. The airfoil has a NACA0012 section. The computational domain has a rectangular shape of 18×14. An isotropic triangular mesh is generated, which has 14,882 elements and 7522 node points. Initially, a steady-state solution is obtained for the airfoil-alone configuration, and then the free vortex is released at 5 chord lengths upstream from the airfoil leading edge and 0.26 chord lengths below the chord line. Calculation is performed by marching the solution in time with a nondimensionalized time step size of 0.00125, which represents the number of chord lengths traveled by the freestream during the time interval. The spatial mesh adaptation is updated at every five time steps.

Figures 7 and 8 show the instantaneous meshes and the corresponding pressure contours at six time levels as the vortex passes by the airfoil. When the vortex is located ahead of the airfoil leading edge, fine cells are concentrated at the vortex location, at the

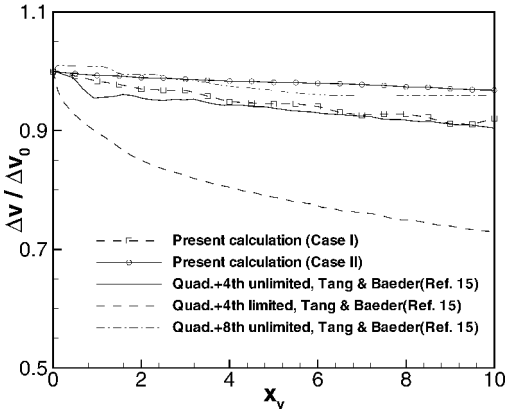

Fig. 6 Decay of normalized peak-to-peak vertical velocity vs convection distance.

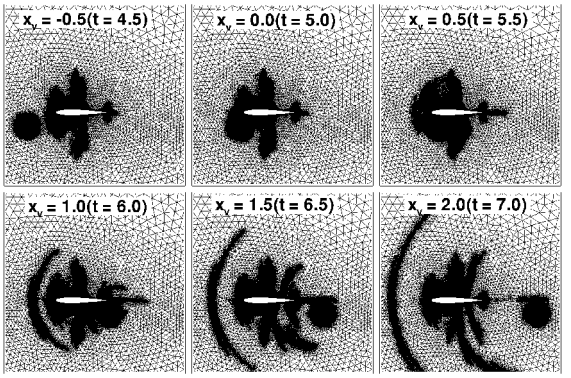

Fig. 7 Instantaneous meshes during BVI for $M_\infty = 0.8$, $a_c = 0.05$, $\Gamma = -0.2$, and $y_v = -0.26$.

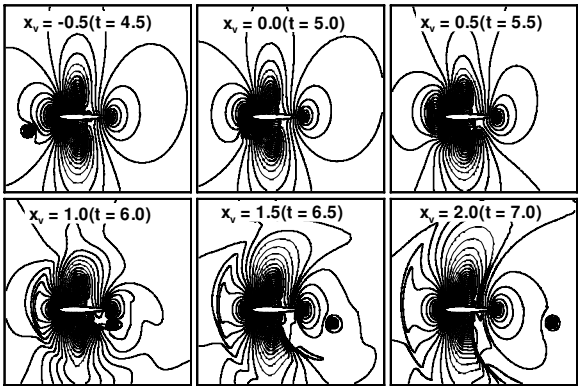

Fig. 8 Instantaneous pressure contours during BVI for $M_\infty = 0.8$, $a_c = 0.05$, $\Gamma = -0.2$, and $y_v = -0.26$.

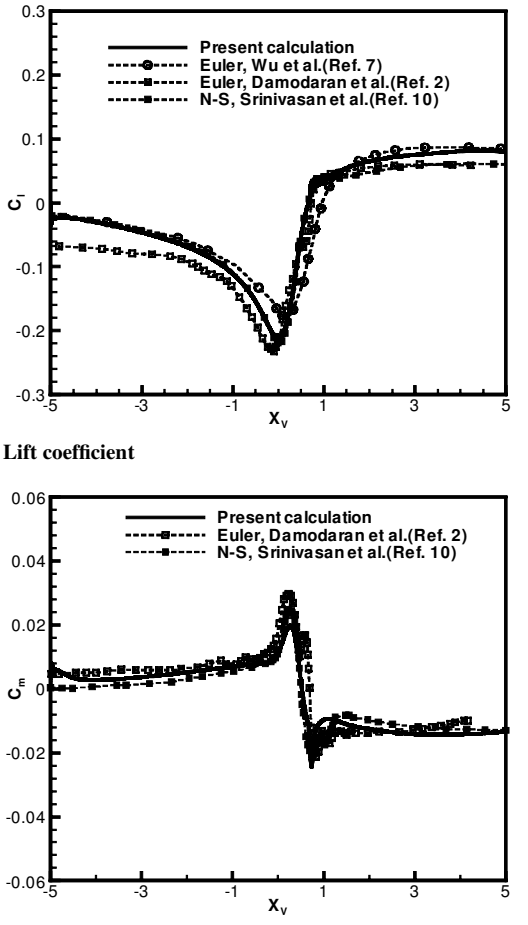

Fig. 9 Comparison of lift and moment variations with instantaneous vortex position for $M_\infty = 0.8$, $a_c = 0.05$, $\Gamma = -0.2$, and $y_v = -0.26$.

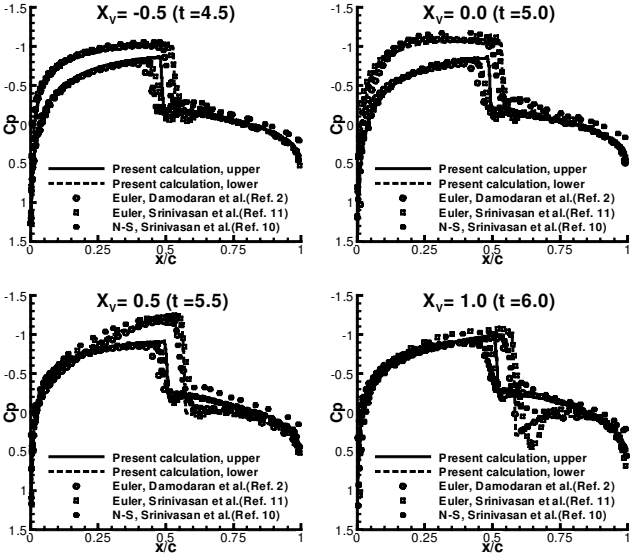

Fig. 10 Comparison of instantaneous airfoil surface pressure distributions during BVI for $M_\infty = 0.8$, $a_c = 0.05$, $\Gamma = -0.2$, and $y_v = -0.26$.

airfoil leading edge, near the trailing edge, and along the shock formation. At this time level, the effect of the vortex is relatively low and the shock waves on the upper and lower surfaces of the airfoil are nearly symmetric. When the vortex is located underneath the airfoil, the shock wave on the lower surface strongly interacts with the vortex and finally bifurcates when the vortex passes by. The time-varying flow physics are also well represented on the dynamically adapted meshes with refined cells near high-gradient regions. The vortex restores its identity downstream of the airfoil trailing edge, which is clearly visible on the pressure contour and also on the corresponding mesh. Even for this weak BVI problem, generation of a compressibility wave and its migration upstream away from the airfoil leading-edge are numerically well predicted using the present solution-adaptive mesh methodology. Figure 9 shows the variation of lift and quarter-chord moment coefficients with the instantaneous streamwise position of the vortex during the interaction process. The lift is initially negative due to the downwash induced by the clockwise vortex located ahead of the leading edge. The lift reaches a negative maximum when the vortex passes near the leading edge and then rapidly increases thereafter. A sudden sign change of the moment from positive to negative is also observed as the vortex travels below the airfoil. The variation of lift and moment coefficients is in reasonably good agreement with those of other Euler and thin-layer Navier–Stokes investigations[2,7,10] based on the perturbation method to alleviate numerical dissipation. Figure 10 shows airfoil surface pressure distributions at selected instantaneous positions of the vortex during the BVI. Good agreement is obtained between the computed results and those of other investigations.[2,10,11] Inviscid calculations, including the present study, predict stronger shock than the viscous simulation on the lower surface after a strong interaction occurs between the vortex and the shock wave at the vortex position of 1.0. This is primarily due to the lack of viscous flow features such as shock/boundary-layer interaction. The present approach captures sharper shock waves due to the solution-adaptive mesh refinement.

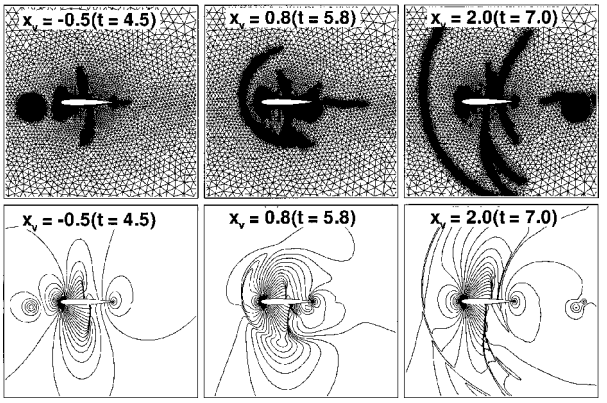

Fig. 11 Instantaneous meshes and corresponding pressure contours during BVI for $M_\infty = 0.8$, $a_c = 0.125$, $\Gamma = -0.5$, and $y_v = -0.1$.

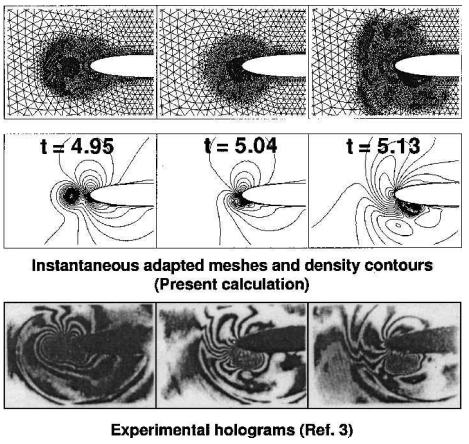

Fig. 12 Close-up view of the vortex–airfoil collision near the leading edge for $M_\infty = 0.5$, $a_c = 0.018$, and $\Gamma = -0.283$.

The second test case of the BVI problem has a stronger interaction between the vortex and airfoil with an offset of -0.1 at a freestream Mach number of 0.8. The vortex has a core radius of $0.125c$ and a nondimensional strength of -0.5. The initial mesh and the computational details are the same as in the earlier BVI problem. The time sequence of the adapted instantaneous meshes and the corresponding pressure contours are shown in Fig. 11. Migration of the vortex, bifurcation of the shock wave, and the formation of acoustic waves are clearly observed not only on the pressure contours, but also on the adapted meshes. It is shown that the leading-edge compressibility wave is generated due to the movement of the leading-edge stagnation point location as the vortex passes the leading edge and subsequently propagates upstream. Also, a transonic acoustic wave is generated on the airfoil lower surface and propagates upstream of the airfoil. When the vortex reaches the trailing edge, another compressibility wave is generated on the upper surface of the airfoil and travels upstream. These waves maintain their identity and strength, not only at the near field, but also away from the airfoil, showing the efficiency and accuracy of the present solution-adaptive scheme.

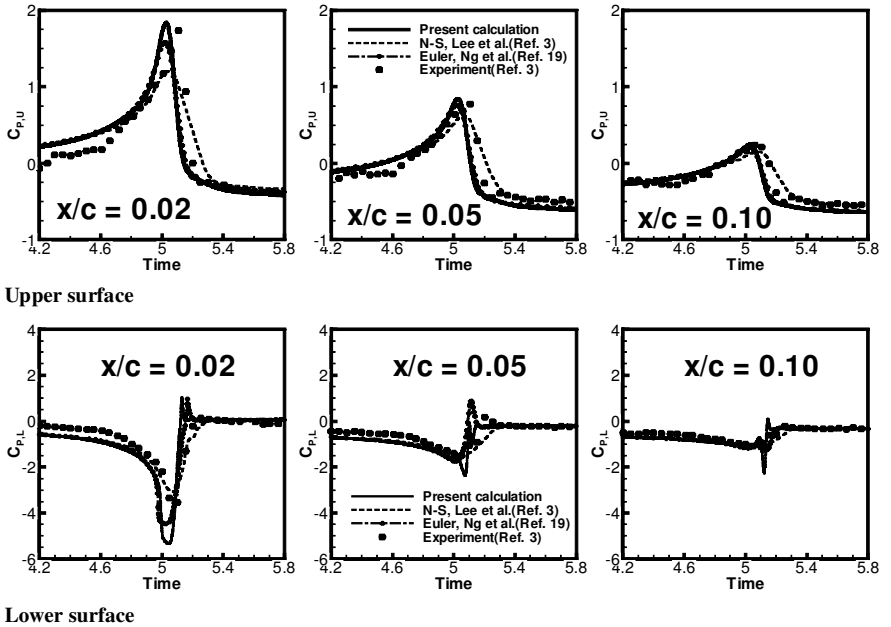

Fig. 13 Comparison of pressure history near the airfoil leading edge for $M_\infty = 0.5$, $a_c = 0.018$, and $\Gamma = -0.283$.

Finally, a vortex–airfoil collision was investigated for a freestream Mach number of 0.5. The vortex has a core radius of $0.018c$ and a nondimensional strength of -0.283. The time-accurate flow simulation is made using a time step size of 0.002.

In Fig. 12, the present computational results are compared with the measurement by Lee and Bershader.[3] It is demonstrated that the behavior of the vortex at and after the collision against the airfoil leading edge is well predicted. The core distortion is clearly observed as the vortex collides with the airfoil leading edge as shown in Fig. 12. The predicted density contours compare well with the experiment within the assumption of inviscid flow. The mechanism of the initial generation of the compressibility wave and its propagation is also well captured. In Fig. 13, comparisons of the surface pressure history near the airfoil leading edge are made at three streamwise locations on both the upper and lower surfaces with the measurement and the Navier–Stokes simulation by Lee and Bershader,[3] as well as with the predicted result of Ng and Hillier.[19] On the upper surface, the current results are in good agreement with the experimental data even though the pressure peak is predicted slightly ahead of the measurement. The magnitude of the pressure peaks and the slope of variation show better agreement with the experiment than other inviscid and viscous results, largely as a result of the enhanced numerical accuracy of the present adaptive meshes. A similar trend is also observed for the lower surface, even though comparisons with the experiment are not as good there as for the upper surface.

Conclusions

A two-dimensional Euler flow solver has been developed for the simulation of unsteady, BVI problems using solution-adaptive unstructured dynamic meshes. The Euler solver is based on a second-order-accurate implicit time integration using a point Gauss–Seidel relaxation scheme and a vertex-centered finite volume method with Roe's flux-difference splitting.[21] For the evaluation of the present solution-adaptive mesh approach, flow around a harmonically oscillating airfoil was calculated, and the results are compared with existing numerical and experimental results. A traveling vortex in a freestream was also simulated to validate the numerical accuracy of the present approach and its ability to minimize the numerical dissipation and to preserve the vortex as it travels downstream. Finally, calculations were made for three BVI problems with varying vortex–airfoil offset distances and freestream Mach numbers. The results show that the interaction between the vortex and the airfoil is well predicted by examining the behavior of shock wave and the vortex. Generation and propagation of acoustic waves are also well predicted. The collision of vortex with the airfoil and the core distortion are also clearly observed, demonstrating that the present approach is an efficient and reliable method for the simulation of close BVI problems.

References

[1]Jones, H. E., "Full-Potential Modeling of Blade-Vortex Interactions," NASA TP-3651, 1997.

[2]Damodaran, M., and Caughey, D. A., "Finite Volume Calculation of Inviscid Transonic Airfoil–Vortex Interaction," *AIAA Journal*, Vol. 26, No. 11, 1988, pp. 1346–1353.

[3]Lee, S., and Bershader, D., "Head-On Parallel Blade–Vortex Interaction," *AIAA Journal*, Vol. 32, No. 1, 1994, pp. 16–22.

[4]Lin, S. Y., and Chin, Y. S., "Numerical Study on Transonic Blade–Vortex Interaction: Flowfield Analysis," AIAA Paper 95-0726, 1995.

[5]Ng, N., and Hillier, R., "Numerical Simulation of the Transonic Blade–Vortex Interaction," *Proceedings of Unsteady Aerodynamics*, Royal Aeronautical Society, London, 1996, pp. 8.1–8.11.

[6]Srinivasan, G. R., and McCroskey, W. J., "Euler Calculations of Unsteady Interaction of Advancing Rotor with a Line Vortex," *AIAA Journal*, Vol. 31, No. 9, 1993, pp. 1659–1666.

[7]Wu, J. C., Hsu, T. M., Tang, W., and Sankar, L. N., "Viscous Flow Results for the Vortex–Airfoil Interaction Problem," AIAA Paper 85-4053, 1985.

[8]Booth, E. R., Jr., "Experimental Observation of Two-Dimensional Blade–Vortex Interaction," *AIAA Journal*, Vol. 28, No. 8, 1990, pp. 1353–1359.

[9]Kalkhoran, I. N., and Wilson, D. R., "Experimental Inveatigation of the Parallel Blade–Vortex Interaction at Transonic Speeds," *AIAA Journal*, Vol. 30, No. 8, 1992, pp. 2087–2092.

[10]Srinivasan, G. R., McCroskey, W. J., and Baeder, J. D., "Aerodynamics of Two-Dimensional Blade–Vortex Interaction," *AIAA Journal*, Vol. 24, No. 10, 1986, pp. 1569–1576.

[11]Srinivasan, G. R., and McCroskey, W. J., "Numerical Simulations of Unsteady Airfoil-Vortex Interactions," *Vertica*, Vol. 11, No. 1, 1987, pp. 3–28.

[12]Steinhoff, J., and Raviprakash, G. K., "Navier–Stokes Computation of Blade–Vortex Interaction Using Vorticity Confinement," AIAA Paper 95-0161, 1995.

[13]Wake, B. E., and Choi, D., "Investigation of High-Order Upwinded Differencing for Vortex Convection," *AIAA Journal*, Vol. 34, No. 2, 1996, pp. 332–337.

[14]Tang, L., and Baeder, J. D., "Time-Accurate Euler Simulation of Vortex Convection," *Proceedings of 52nd Annual Forum of the American Helicopter Society*, American Helicopter Society, Alexandria, VA, 1996, pp. 1489–1499.

[15]Tang, L., and Baeder, J. D., "Accurate Euler Simulation of Parallel Blade–Vortex Interaction," *Proceedings of 53rd Annual Forum of the American Helicopter Society*, American Helicopter Society, Alexandria, VA, 1997, pp. 708–718.

[16]Holmes, D. G., and Connell, S. D., "Solution of the Two-Dimensional Navier–Stokes Equations on Unstructured Adaptive Grids," AIAA Paper 89-1932, 1989.

[17]Rausch, R. D., Batina, J. T., and Yang, H. T. Y., "Spatial Adaptation of Unstructured Meshes for Unsteady Aerodynamic Flow Computations," *AIAA Journal*, Vol. 30, No. 5, 1992, pp. 1243–1251.

[18]Richter, R., and Leymond, P., "Precise Pitching Airfoil Computation by Use of Dynamic Unstructured Meshes," AIAA Paper 93-2971, 1993.

[19]Ng, N., and Hillier, R., "Numerical Simulation of the Transonic Blade–Vortex Interaction," AIAA Paper 97-1846, 1997.

[20]Hwang, C. J., and Kuo, J. Y., "Adaptation Finite Volume Upwind Approaches for Aeroacoustic Computations," *AIAA Journal*, Vol. 35, No. 8, 1997, pp. 1286–1293.

[21]Roe, P. L., "Approximate Riemann Solvers, Parameter Vectors, and Difference Schemes," *Journal of Computational Physics*, Vol. 43, No. 2, 1981, pp. 357–372.

[22]Rango, S. D., and Zingg, D. W., "Implicit Navier–Stokes Computations of Unsteady Flows Using Subiteration Method," AIAA Paper 96-2088, 1996.

[23]Anderson, W. K., "An Implicit Upwind Algorithm for Computing Turbulent Flows on Unstructured Grids," *Computers and Fluids*, Vol. 23, No. 1, 1994, pp. 1–21.

[24]Venkatakrishnan, V., "Accuracy of Limiters and Convergence to Steady-state Solutions," AIAA Paper 93-0880, 1993.

[25]Batina, J. T., "Implicit Flux-Split Euler Schemes for Unsteady Aerodynamic Analysis Involving Unstructured Dynamic Meshes," *AIAA Journal*, Vol. 29, No. 11, 1991, pp. 1836–1843.

[26]Landon, R. H., "NACA0012 Oscillatory and Transient Pitching," *Compendium of Unsteady Aerodynamic Measurements*, R-702, AGARD, 1982.

S. K. Aggarwal
Associate Editor